

Saturation mechanisms for edge turbulence

D. A. Russell, J. R. Myra and D. A. D'Ippolito

Lodestar Research Corporation, Boulder, Colorado

July 2009

submitted to *Physics of Plasmas*

DOE/ER/54392-54

LRC-09-130

LODESTAR RESEARCH CORPORATION

*2400 Central Avenue
Boulder, Colorado 80301*

Saturation mechanisms for edge turbulence

D. A. Russell,[†] J. R. Myra and D. A. D'Ippolito

Lodestar Research Corporation, 2400 Central Avenue, Boulder, Colorado 80301

Abstract

Saturation mechanisms for two-dimensional (2D) edge turbulence are studied in a Braginskii-type fluid model using the Scrape-Off-Layer Turbulence (SOLT) code. The simulations study the interaction of edge and scrape-off-layer (SOL) turbulence, blob generation, momentum transport and shear flow generation in 2D turbulence. It is shown that a key parameter is the zonal flow shear damping rate, which controls both the level of saturated turbulence and the rate of blob generation. The flow shear profile is produced by a combination of the turbulent Reynold's stress inside the last closed surface and the sheath-induced flow in the SOL. The turbulent properties are studied as a function of zonal flow damping. The role of other edge and SOL dissipation mechanisms are also discussed.

PACS numbers: 52.35.Ra, 52.35.Kt, 52.55.Fa, 52.65.Kj

[†]email: dave@lodestar.com

I. Introduction

There has been a great deal of research on the mutual interaction between *core turbulence* and nonlinear structures (sheared zonal flow and radial streamers) in tokamaks and in other plasma confinement devices. For background and references, the reader is referred to the excellent review articles in Refs. [1-3]. Theory, simulations and experiment all point to an emerging paradigm which explains many aspects of global confinement in tokamaks. In the limit of small dissipation (low collisionality), turbulence generates strong zonal flows (ZF) which act back on the turbulence and saturate the turbulent radial transport at low levels.⁴ If the dissipation is strong enough, the flows are suppressed and radial streamers form, which produce rapid radial transport. In the context of core turbulence, the radial streamers produce bursty transport^{5,6} and may be associated with self-organized criticality (SOC) or avalanche phenomena.⁴ The connection of this transport to the edge and scrape-off-layer (SOL) plasmas has not been established yet.

There has also been a rapidly growing body of related work on *edge turbulence*, including both experimental measurements⁷⁻¹⁹ and computer simulations.^{13,20-27} (A recent review of edge turbulence measurements has been given in Ref. 28.) The experiments and computer simulations show that some of the concepts developed to explain core turbulence also apply to the edge and SOL. Some of the key edge simulation results include turbulent transport by radial streamers,^{21,24,25} turbulent generation of sheared flow without external momentum input,²⁰⁻²⁷ regulation of turbulent transport by sheared flow,²⁰⁻²⁷ regimes of bursty transport,^{22,24} dependence of the turbulent saturation mechanism on various sources of dissipation,²¹⁻²⁶ regulation of streamer break-up (and thus blob generation) by sheared flows,²⁴ correlation of particle and momentum transport,²⁶ and regimes of low and high transport.²⁷ These features appear to be relatively robust, appearing in simulations with different dimensionality (2D or 3D), geometry (cylindrical or toroidal), instability drives, damping mechanisms, etc.

There are also differences between core and edge transport. The dominant linear instabilities are different in the core and edge. Also, edge turbulence is “stronger” in the sense that the fluctuations are order unity compared to the background. This gives rise to the phenomena of “blob” generation^{29,30} and convective transport in the SOL. (For more details, see the recent comprehensive reviews of blob theory³¹ and related experimental measurements.²⁸) The blobs or streamers are generated at the location of the maximum linear growth rate as part of the turbulence saturation process. If the sheared zonal flows are not too strong, the blobs transport particles, heat and momentum, and thus interact in a complicated way with the flow profile. Another feature of edge turbulence is that there is no scale separation between the background equilibrium and the turbulent fluctuations. Finally, the turbulence spans two radial regions with different topologies (closed field lines inside the last closed surface (LCS), and open field lines outside the LCS in the SOL). The field lines in the SOL terminate in sheaths at material surfaces (such as divertor plates) and sheath effects are important. One of the themes of the present paper is that sheath-driven sheared flows can interact in a non-local way with the sheared flow produced by the turbulence.

In this paper, we will discuss the interaction of edge turbulence, blob generation, momentum transport and sheared zonal flows in two-dimensional (2D) fluid simulations using a Braginskii-type model for the edge and SOL. The goal is to unify a number of the results discussed previously and generalize them to include the effects of edge and SOL dissipation. The simulations are done with the 2D “Scrape-Off-Layer Turbulence” (SOLT) code. The code includes the physics of drift wave and curvature-driven interchange modes, sheared zonal flows in a momentum-conserving treatment, flow damping (e.g. applicable to ion-neutral collisions), and sheath dissipation in the SOL. Since the code is global (not a flux-tube model) there is no scale separation between the equilibrium gradients and the turbulent scales. The profiles are free to evolve nonlinearly with $\delta n/n \sim 1$ (and similarly for the other fields) so that the physics of blob generation

and transport can be studied. The inclusion of passive (blob) transport of perpendicular momentum²⁶ and sheath dissipation of momentum are two of the unique features of this code.

Some important results of the present work are:

- (1) The damping rate of the sheared flow is the control parameter determining the mechanism of edge turbulence saturation. The magnitude of the turbulent flux, the degree of intermittency, and the spatial scales all depend on the control parameter.
- (2) There are three physical regimes of nonlinear saturation depending on the strength of the zonal flow damping, including a bursty regime in the case of weak damping.
- (3) Sheared flow also plays an important role in blob creation. A transition from radial streamers to blobs occurs as the flow damping parameter is decreased, allowing flow shear to tear apart the streamers. The simulation results confirm a previously postulated streamer breakup condition²⁴ and relate this condition to the saturation regime.
- (4) The sheared flow at the LCS is driven by two sources at different radial locations: the turbulent Reynold's stress (inside the LCS) and the sheath-induced flow (outside the LCS). Their competition gives reduced velocity shear in the main interaction region and can lead to bursty transport when \bar{v}'_y is small in this layer.

II. Simulation Model

The 2D SOLT code simulates turbulence driven by magnetic curvature and drift wave effects in a 2D plane normal to the magnetic field \mathbf{B} . The simulation domain is the outer midplane of the tokamak, encompassing both the edge and SOL regions. The present version of the code is similar to the one used in Ref. 26, generalized to a three-field (Φ, n_e, T_e) model. A previous version of the code^{32,33} included the coupling along the magnetic field \mathbf{B} to another 2D plane representing the X-point region, but this effect is not retained here. The present model includes the effects of wave phase directionality

(drift-waves), curvature drive, radial transport (turbulent Reynolds stress and blobs), sheared flows, and dissipation (sheath loss and friction). Note that the drift-wave physics plays a role in producing a sheared flow layer in this model because it gives the turbulence a directionality. A zonally-averaged momentum conservation law is used to advance the zonal flows. The physics of the model is described in more detail in an earlier paper²⁶ and a derivation of the equations is given in Appendix A of that paper. The code uses local coordinates (x, y, z) for the radial, binormal (approximately poloidal) and parallel directions, where $x \equiv \Delta r = r - r_s$ is the radial distance from the nominal last closed surface, defined at the outer mid-plane with $\Delta r > 0$ in the SOL. In this paper, we will use x and Δr interchangeably.

The SOLT code evolves dimensionless equations for the electron density n , electron temperature T , vorticity $\nabla^2 \tilde{\Phi}$ (yielding the fluctuating potential $\tilde{\Phi}$), and the zonally-averaged poloidal momentum $p_y \equiv \langle n v_y \rangle$, which have been obtained by integrating the fundamental conservation relations along the magnetic field and using model closures for the parallel physics.²⁶ The total density and temperature satisfy

$$\frac{dn}{dt} = \alpha_{dw} \bar{T}^{3/2} \left\{ \Phi - T \ln n \right\} - \alpha_{sh} n T^{1/2} e^{(\Phi_B - \Phi)/T} + D \nabla^2 n + S_n, \quad (1)$$

$$\frac{dT}{dt} = -\alpha_{sh} S_E T^{3/2} e^{(\Phi_B - \Phi)/T} + S_T, \quad (2)$$

the fluctuating (i.e. y -dependent) potential is determined by

$$\frac{\partial}{\partial t} \nabla^2 \tilde{\Phi} + \left\{ \nabla \cdot \nabla \nabla^2 \Phi \right\} = \left\{ \alpha_{dw} \frac{\bar{T}^{3/2}}{\bar{n}} (\Phi - T \ln n) + \alpha_{sh} T^{1/2} \left(-e^{(\Phi_B - \Phi)/T} \right) - \frac{\beta}{n} \frac{\partial(nT)}{\partial y} + \mu \nabla^4 \Phi \right\}, \quad (3)$$

and the zonally-averaged poloidal momentum $p_y \equiv \langle n v_y \rangle$ satisfies

$$\frac{\partial p_y}{\partial t} + \frac{\partial}{\partial x} \langle n v_x v_y \rangle = - \int_x^{L_x} dx \alpha_{sh} \langle n T^{1/2} (1 - e^{(\Phi_B - \Phi)/T}) \rangle + \bar{\mu} \frac{\partial^2}{\partial x^2} \bar{v}_y - \mathbf{v}_{p_y} p_y \quad , \quad (4)$$

where $d/dt = \partial/\partial t + \mathbf{v} \cdot \nabla$ and $\mathbf{v} = \mathbf{b} \times \nabla \Phi$ describes convection in the constant background magnetic field, $\mathbf{B} = B\mathbf{b}$. We have set $T_i = 0$ in this model. Each field quantity Q is expressed as $Q = \bar{Q} + \tilde{Q}$, where $\bar{Q} \equiv \langle Q \rangle \equiv \int dy Q / \int dy$ is the zonally-averaged piece and $\tilde{Q} = Q - \bar{Q}$ is the fluctuating piece. For convenience in notating the nonlinear terms, we have also defined a bracket notation for the zonal average, $\langle AB \rangle = \int dy AB / \int dy$, and for the fluctuating part, $\{AB\} = AB - \langle AB \rangle$. Finally, for later use we define the time average $\langle Q \rangle_t = \int dt Q / \int dt$. An ensemble average is obtained by averaging over both y and t , $\langle \bar{Q} \rangle_t$.

In Eqs. (1)-(4) and throughout the remainder of the paper we employ dimensionless (Bohm) units

$$\Omega t \rightarrow t, \quad S/\Omega \rightarrow S, \quad \mathbf{x}/\rho_s \rightarrow \mathbf{x}, \quad e\Phi/T_{ref} \rightarrow \Phi, \quad n/n_{ref} \rightarrow n, \quad T/T_{ref} \rightarrow T \quad (5)$$

where $\Omega = ZeB/m_i c$, $\rho_s = c_s/\Omega$ with $c_s^2 = T_{ref}/m_i$, and n_{ref} and T_{ref} are reference values of the density and electron temperature defined subsequently. The dimensionless electron adiabaticity parameter α_{dw} , sheath conductivity α_{sh} and curvature β are defined by

$$\alpha_{dw} = \frac{2\rho_s m_i c_s}{L_{||e}^2 \nu_{ei0} m_e}, \quad \alpha_{sh} = \frac{2\rho_s}{L_{||s}}, \quad \beta = \frac{2\rho_s}{R} \quad . \quad (6)$$

where ν_{ei0} is a typical value of the electron-ion collision frequency, and in Eq. (6) all quantities are evaluated at T_{ref} .

We now discuss the physical interpretation of the various terms. The terms involving α_{dw} in Eqs. (1) and (3) model the electron response (i.e. the parallel current) on closed surfaces; taking α_{dw} large enforces adiabatic electrons. Note that the zonal average of these terms vanishes. The quantity $L_{||e}$ is a typical parallel scale length for the turbulence in the edge plasma, usually taken as the connection length $L_{||} \sim qR$, where q is

the safety factor and R the major radius of the torus. We take $\alpha_{\text{dw}} = \alpha_{\text{dw}}(x)$ to decay rapidly in the SOL, reflecting the strong increase in collisionality.

In the SOL, the electron response is modeled by the α_{sh} terms, where $\alpha_{\text{sh}}(x)$ vanishes in the core and $L_{\parallel\text{s}}$ is the parallel connection length in the SOL to the sheaths. The α_{sh} terms in Eqs. (1) to (4) represent the sheath end-loss for particles, energy, charge and poloidal momentum. We use the full exponential form of the sheath terms, valid for arbitrary Φ/T . The Bohm potential used in this term is given by $\Phi_{\text{B}} = T \ln v \approx 3T$, where $v = (m_i / 2\pi m_e)^{1/2}$. In Eq. (2), s_{E} denotes the sheath energy transmission coefficient. The integrated sheath term^{26,34} in Eq. (4) describes the $\mathbf{J} \times \mathbf{B}$ force from the radial current in the current loop implied by $\nabla \cdot \mathbf{J} = 0$, because there is parallel current flow into the sheaths, i.e. $\langle J_x \rangle = -\int_0^x dx' \langle \nabla_{\parallel} J_{\parallel} \rangle$. As emphasized in our earlier work,²⁶ the sheath dissipation term is necessary to allow a spontaneous generation of perpendicular momentum in the core.

The field-line-integrated curvature drive is modeled by the β term. The model thus incorporates elements of the classical drift-wave model of Wakatani-Hasegawa³⁵ (α_{dw}) in the edge plasma and the blob model equations^{29,30} (α_{sh} and β) describing convective transport in the SOL plasma. Note that Eq. (4) preserves momentum conservation for the zonally averaged flows, i.e. it does not use the Boussinesq approximation that is used in Eq. (1). This is an important and unique feature of the model.

The dissipation terms involve the following dimensionless coefficients: diffusion D , hyperviscosity μ , viscosity $\bar{\mu}$ and flow damping ν_{p_y} . In the present paper, the first three dissipation terms will be included primarily for numerical purposes but the last coefficient will be regarded as physical. For example, for cool plasmas and high neutral background densities (such as in small scale experiments or near the tokamak divertor plates) ν_{p_y} is due to ion-neutral collisions. We will show that there is an interesting dependence of the turbulence on the flow damping parameter.

The particle and heat source terms (S_n, S_T) are taken as:

$$S_n(x) = v_n(x)(n_0(x) - n) , \quad S_T(x) = v_T(x)(T_0(x) - T) , \quad (7)$$

where $v_n(x)$ and $v_T(x)$ are tanh functions which vanish in the SOL, thereby defining the last closed surface (LCS). In the limit of large v_n and v_T , the profiles are clamped in the edge, i.e. $n \rightarrow n_0(x)$ and $T \rightarrow T_0(x)$, where $n_0(x)$ and $T_0(x)$ are reference profiles for the electron density and temperature. The absence of a momentum source term $\propto v_y S_n$ in Eq. (4) implies that S_n replaces lost particles in Eq. (1) but not momentum in Eq. (4), i.e. the source creates plasma at zero velocity rather than at the local ambient velocity. The fact that particles lost at finite v_y in the SOL are replaced by particles with $v_y = 0$ in the edge implies a loss of v_y which is mediated by the passive transport of momentum by blobs, another important feature of the present model.

Thus, the simulation domain contains two radial regions defined by the source and sink profiles, as shown in Fig. 1: (i) the *edge* region inside the separatrix ($\Delta r < 0$) is characterized by non-zero particle and energy source profiles and by drift-wave physics where $\alpha_{dw}(x)$ is finite; (ii) the *far SOL* ($\Delta r > 5$ cm) is defined by a finite sheath conductivity profile $\alpha_{sh}(x)$. There is an intermediate region (*near SOL*) where both α_{dw} and α_{sh} are small; this simulates the region near the separatrix, where the parallel connection length is long ($L_{||} \propto 1/\alpha_{sh} \rightarrow \infty$). The left boundary of the simulation represents the matching of the edge to the core plasma, and the right boundary represents the location of the wall bounding the SOL plasma.

The model equations are solved subject to the following set of boundary conditions (BC): (1) poloidal (i.e. y) periodicity is assumed; (2) fluctuations are assumed to vanish ($\tilde{n} = \tilde{T} = \tilde{\Phi} = 0$) on the radial (left and right) boundaries; (3) $\bar{\Phi}$ is held constant and p_y is freely evolved on the core side (left) boundary; (4) the following conditions are imposed at the wall (right) boundary: $n = n_{wall}$, $T = T_{wall}$, and $p_y = 0$.

Our computational model is similar to the one used by Bisai et al.²⁴ with two additional features. The electron temperature equation is evolved here, and a separate momentum conserving equation is used here to accurately describe the evolution of the y-momentum. As discussed subsequently, this equation treats the passive (blob) momentum convection term,²⁶ which is not usually included in edge turbulence simulations.

III. Simulation Results

In this section, we describe results from 2D turbulence simulations carried out using the model described in Sec. II.. The purpose of these simulations was to investigate the physical mechanisms responsible for nonlinear saturation of the turbulence. The study presented here focuses on the scaling of the turbulence with the flow damping parameter v_{py} in Eq. (4). The results show that the flow damping rate is a key control parameter for the turbulence²⁵ and we find that there are regimes of intermittency near marginality, depending on the core-side potential, $\bar{\Phi}(0)$. A set of “rules” which explain the simulation results will be discussed in Sec. IV.

A. Moderate instability drive, full range of damping

We will use the following parameters as a base case: deuterium plasma, $B = 2500$ G, $R = 150$ cm, $\rho_s = 0.62$ cm, $L_x = L_y = 100 \rho_s$, $n_{\text{ref}} = 10^{13}$ cm⁻³, $n_{\text{wall}} = 2 \times 10^{11}$ cm⁻³, $T_{\text{ref}} = 117$ eV, $T_{\text{wall}} = 2.8$ eV, $c_s = 75$ km/s; dimensionless: $\alpha_{\text{DW}} = 0.26$, $\alpha_{\text{sh}} = 2.4 \times 10^{-2}$, $\beta = 8.3 \times 10^{-3}$, $\mu = 0.1$, $\mu_{\text{bar}} = 0.01$, $D = 0.01$, $s_E = 6$. The dimensionless source rates v_n and v_T , Eq. (7), are similar in shape to their respective reference profiles, $n_0(x)$ and $T_0(x)$, shown in Fig. 1, and each rate has a maximum value ($x \rightarrow -\infty$) of 0.01. For this base case, the value of β corresponds to moderate instability drive, and the flow damping parameter v_{py} is varied from 0 to ∞ . Choosing much smaller values of β does not lead to sustainable turbulence, and the case of larger β is discussed subsequently. The base case parameters and profiles used here are similar to those of a low power, low-confinement-mode discharge in the National Spherical Torus Experiment (NSTX).³⁶

First, we summarize the results for the limiting cases. In the limit $\nu_{py} \rightarrow 0$, the zonal flow is strong, the turbulence saturates at a relatively low level and produces convecting objects that look blob-like. The time-history of the turbulent flux shows *intermittent* bursts, and the turbulence saturates as a result of the stabilizing effect of the *sheared flows*. In the limit $\nu_{py} \rightarrow \infty$, the zonal flow is absent, the turbulence saturates at a relatively high level, and it produces convecting objects that look more like radial streamers than blobs. This suggests that the sheared flows are necessary for the blob creation process,²⁴ as discussed subsequently. The time-history of the turbulent flux shows *quasi-periodic* oscillations, and it appears to saturate by *wave-breaking*, i.e. the condition $\langle \nabla \delta n_{\text{rms}} / \nabla \bar{n} \rangle_t \sim 1$ is satisfied near the surface of maximum growth rate. Physically, this condition is satisfied because the large turbulent flux causes density plateau formation outside the LCS, reducing $\nabla \bar{n}$. The time history of the particle flux, $\Gamma(t)$, is shown for the two limiting cases in Fig. 2. The quasi-periodic behavior observed in the absence of shear flow ($\nu_{py} = \infty$) is due to the beating of drift waves resonant with the enduring phalanx of radial streamers created by the interchange instability. If the drift waves are eliminated from this simulation, the system relaxes to a single streamer, no quasi-periodic oscillations are observed, and the radial flux doubles; drift waves inhibit this cascade. The details of this state depend on the size of the simulation, but the rapid transport by radial streamers is universal.

To illustrate the transition between the limiting cases, we have computed the dependence of the zonal flow shear and the turbulent radial particle flux as a function of the flow damping parameter ν_{py} . We plot the dependence of flow-shear and the radial particle flux vs ν_{py} in Fig. 3, where $\xi \equiv d\bar{v}_y/dx$ is the zonally-averaged flow shear in the binormal (approximately poloidal) direction, and $\bar{\Gamma} = \langle n v_x \rangle$ is the zonally-averaged particle flux. (See the caption for details of this measurement.) The shear is computed at the LCS, $\Delta r = 0$; the particle flux is measured at the “sheath position”, $\Delta r = 4.42$ cm (see Fig. 1). Figure 3 shows that there is a smooth but rapid transition from the sheared-flow to the wave-breaking regime as ν_{py} increases. This transition encompasses two regimes

with different turbulence saturation physics. The turbulent particle flux across the LCS (not shown) is also much lower for small flow damping than in the opposite limit. Thus, in terms of SOL transport, the large- v_{py} limit is a “low-confinement” regime whereas the small- v_{py} limit gives a “high-confinement” regime. An analogous transition has been seen in other simulations.²⁷

In the weak-damping regime (small v_{py}), the turbulence is saturated by the sheared flows. To demonstrate this, we carried out a numerical experiment, illustrated in Fig. 4. The simulation was interrupted at a certain instant of time and the self-consistent shear profile $\xi(\Delta r)$ was calculated; this is the solid curve shown in Fig. 4(a). A prescribed, time-dependent shear profile was constructed by adding a sinusoidal perturbation, $\delta v_y \sim \sin \omega t$, localized to the birth zone by a Gaussian radial envelope, to the time-independent reference profile, which generates the dashed curves in Fig. 4(a) at times of maximum departure from the reference profile. The Gaussian perturbation is centered in the region $-5 \text{ cm} < \Delta r < 0 \text{ cm}$, where the gradients and linear growth rates of the underlying instabilities are maximized, and the sheared flows are most effective in moderating the turbulence. This is also the blob birth zone. The simulation was re-started with the synthetic flow profile. The plus and minus symbols in Fig. 4(b) indicate the times when the corresponding profiles of Fig. 4(a) occur in the simulation. The results in Fig. 4(b) show that the level of turbulence is *enhanced* when the magnitude of the local velocity shear $|\xi|$ is below an apparent threshold, and the turbulence level is *reduced* dramatically when the magnitude of the velocity shear exceeds that threshold. These results demonstrate that turbulence saturation occurs by the stabilizing effects of sheared zonal flows in the weak damping limit ($v_{py} \rightarrow 0$).

In the strong-damping regime ($v_{py} \rightarrow \infty$), the zonal flows are suppressed, and the turbulence saturates by means of density profile modification, viz. the formation of a pressure plateau near the LCS. The required profile modification is given by the “wave-breaking” condition $\langle \nabla \delta n_{\text{rms}} / \nabla \bar{n} \rangle_t \sim 1$, evaluated near the surface of maximum

growth rate. Without the stabilizing effect of sheared zonal flows, the turbulence grows to high levels, producing a large increase in the turbulent radial particle flux at the LCS and a plateau in the density and temperature profiles (see Fig. 5) as v_{py} increases. Figure 5 shows that only a small amount of damping is needed to produce a significant density plateau in the near SOL. In this limit, the nonlinear evolution of the density profile saturates the turbulence by reducing the instability drive. Similar behavior was found in the “low confinement” regime described in Ref. 27.

B. Marginality (bursty regime)

In the previous section, two turbulence regimes were discussed, one regulated by sheared zonal flows (at small v_{py}) and one regulated by plateau formation (at large v_{py}). Both regimes were studied in simulations that were sufficiently above threshold for strong turbulence that intervals of relative quiet between turbulent bursts were seldom observed. But when such bursts did occur (as in the intermittent, low- v_{py} cases described above) the quiet intervals were not so long as the bursts themselves. In the case described below, and in many other turbulence models, as a threshold is approached from the turbulence side, the quiescent periods grow longer and the bursts grow more intense.

The model has several parameters that control the intensity of the turbulence and the nature of the intermittency. For example, the curvature drive strength (β) and dissipation rates of fluctuations (α_{sh} , D , μ , v_n , v_T) can be competed to fine-tune the quality of the turbulence near threshold. Here, however, we focus on the increased intermittency that results when the core-side boundary potential, $\overline{\Phi}(0)$, is raised relative to its limiting value at the wall boundary, $\overline{\Phi}(L_x)$. If the difference between these two boundary values is sufficiently large, the system is stabilized by the strong, ambient sheared flow associated with the radial electric field. Though the sheath absorption profile, $\alpha_{sh}(x)$, plays an important role in this stabilization, as it determines the shape of

the sheared flow profile in the near-SOL and birth zone, we defer a more thorough study of that role to a future publication and keep the sheath profile of Sec. III A.

We plot the time history of the zonally-averaged particle flux $\bar{\Gamma}(t)$ at the entrance to the sheath ($\Delta r = 4.4 \text{ cm}$) in Fig. 6 for two values of the core-side potential, $\bar{\Phi}(0)$, and $v_{py} = 0$. We see the appearance of quiescent intervals between large bursts of particle flux for the case with the larger boundary potential but note that the time-averaged flux is nearly the same in each case and that the initial burst for the lower boundary potential is about as strong as the isolated bursts for the higher potential. In the latter case the system is reset more nearly to the initial condition following a burst.

A survey of the effect of flow damping for the higher- $\bar{\Phi}(0)$ case yields a particle flux curve similar to that in Fig. 3 but with smaller fluxes for non-zero v_{py} because the boundary conditions for this case impose a stronger overall shear on the velocity profile.

To explore the origin of the bursts, in Fig. 7 we plot a 500 μs time slice of the $\bar{\Phi}(0) = 10$ simulation, showing the time history of the particle flux $\Gamma = \langle nv_x \rangle$, the velocity shear $\xi = d\bar{v}_y/dx$, and the zonally-averaged pressure gradient $dp/dx = d(\bar{nT})/dx$. In contrast to Fig. 6, the values plotted in Fig. 7 are computed inside the LCS at $\Delta r = -2 \text{ cm}$. First, we see that dp/dx and Γ are both “bursty” with a burst time scale of about 10 μs (small bumps) over a burst interval of 100 μs . Second, we observe that the shear ξ is negative during the quiet interludes, but changes sign during the burst, and thus there are several times at which $\xi = 0$. In fact, the bursts occur close to the times when the velocity shear passes through zero. Similar behavior is observed in the artificial model problem described above (See Fig. 4.), but here the shear flow evolves self-consistently. The bursts of particles reduce the pressure gradient in the birth zone and outside the LCS in the near-SOL, forming a density plateau.

The velocity shear profile is plotted in Fig. 8 at times preceding and including a burst. There are two classes of zero-shear points observed in the simulations. Those which are perturbed but not destroyed by the bursts and those which come and go with,

and are directly responsible for, the bursts. The latter lie within the birth zone ($-4 \text{ cm} < \Delta r < 0 \text{ cm}$ in Fig. 8). The former lie outside the birth zone and are found, approximately, by solving the momentum equation (4) in the absence of turbulence (zero momentum flux) as a boundary- and as an *initial*- value problem, e.g., following a burst. This quiescent profile may evolve so as to extinguish the turbulence unless there is sufficient residual Reynolds flux to maintain the negative shear flow layer in the birth zone between bursts.

The zero-shear points associated with bursts are created *locally* by the growing unstable modes in the birth zone: a radially-localized perturbation of the zonal flow will introduce such points if its amplitude is sufficiently large. Since the instability is moderated by the flow shear, the rate at which the amplitude grows increases with the amplitude, resulting in a burst. This is a self-consistent, nonlinear burst, unlike the manufactured, linear surges of Fig. 4.

C. Role of blobs

Next, we examine the physics of blob generation in our simulation. One postulated mechanism of blob creation is that of radial streamer break-up by sheared flows. The following condition for streamer break-up was proposed in Ref. 24:

$$\tau_s < \tau_x \quad (8)$$

where $\tau_s \sim a_y / \Delta v_y$ is the timescale for shearing the radial streamer, $\Delta v_y \sim (\partial v_y / \partial x) a_x \equiv v'_y a_x$ is the maximum velocity shear, a_x and a_y are the radial and poloidal dimensions of the streamer structure, and a prime denotes a radial derivative. The radial convection time is given by $\tau_x \sim a_x / v_x$. Combining these results gives the following heuristic condition for streamer break-up²⁴

$$\frac{v'_y}{v_x} a_x^2 > a_y \quad . \quad (9)$$

Taking the simple limit of symmetric blobs, $a_x \sim a_y \equiv a_b$, Eq. (9) says that blobs form when $a_b v'_y > v_x$.

Here we extend this result by making a few additional self-consistent estimates. First, we use the blob “correspondence principle”³⁷ (also sometimes referred to as the blob dispersion relation), which states that there is a correspondence between the linear instability parameters (γ , k_\perp , k_\parallel , L_n) and nonlinear blob parameters (v_x , a_b , L_\parallel) given by

$$\gamma \rightarrow \frac{v_x}{a_b}, k_\perp \rightarrow \frac{1}{a_b}, L_n \rightarrow a_b, k_\parallel \rightarrow \frac{1}{L_\parallel} . \quad (10)$$

(A simulation test of this principle is illustrated in Fig. 2 of Ref. 32.) Assuming symmetric blobs and using the first rule, $v_x = \gamma a_b$, the condition for streamer break-up reduces to

$$v'_y > \gamma \quad (11)$$

But this is precisely the condition for the shear-flow stabilization regime to win out over the plateau (“wave-breaking”) regime, and as we will show, the equality $v'_y \sim \gamma$ corresponds to the “knee” of the $\Gamma(v_{py})$ curve shown in Fig. 3. Note that this analysis implies that streamers would persist in the strong-damping regime ($v_{py} \rightarrow \infty \Rightarrow v'_y \rightarrow 0$), as observed in our simulations.

In summary, our simulations are consistent with the idea that radial streamers are broken up by strong sheared flows, and this process emits blobs which propagate across the SOL. The condition for blob formation is identical to the condition that the turbulence saturation be provided by the sheared zonal flows. Since radial streamers provide more continuous radial transport than do intermittent blobs, one would expect the turbulent particle flux Γ to be larger in the weak sheared-flow regime, which is consistent with the behavior observed in Fig. 3.

D. Role of dissipation

Another important result from the SOLT simulations is the effect of dissipation in the SOL on the turbulence level inside the LCS. There is a non-local coupling of edge plasma and SOL which comes about from the first two terms on the rhs of the poloidal momentum equation, Eq. (4).

The first term describes dissipation in the sheaths and tends to force the electrostatic potential to its Bohm value in the SOL. This loss term is a sink for the momentum transported across the LCS.²⁶ (There are also corresponding sheath loss terms in the equations for n , T , and $\tilde{\Phi}$.) Recent comparisons of SOLT code simulations with NSTX turbulence data showed that the agreement was sensitive to the details of the sheath term, implying that the sheath dissipation played an important role in regulating the turbulence.³⁸

The second term describes diffusive momentum transport, e.g. by neoclassical or classical effects. This term causes turbulence-induced sheared flows to diffuse from the edge into the core,²⁶ and also allows sheath-induced sheared flows in the SOL to diffuse back into the edge, where it acts back on the turbulence. If \bar{u} is large enough, the turbulence is completely stabilized in our simulations, leading to a quiescent state. The role of this term in regulating turbulence was studied previously.²¹

The overall picture that emerges is that the velocity shear profile, $\overline{v}_y'(x)$, is a balance between the effects of the turbulence (Reynolds stress) induced flow in the edge plasma and the sheath-induced flow in the SOL. These two sources are coupled by the diffusion term.

There is also a strong dependence of the turbulence on the shear flow damping [third term on the rhs of Eq. (4)], as illustrated in Fig. 3. A detailed discussion of this effect is given in the next section.

IV. Theory of turbulence saturation regimes

In this section, we investigate the parameter regimes uncovered by the simulations described in Sec. III. We begin by examining the poloidal momentum equation, reproduced here for convenience:

$$\frac{\partial p_y}{\partial t} + \frac{\partial}{\partial x} \langle n v_x v_y \rangle = - \int_x^{L_x} dx \alpha_{sh} \langle n T^{1/2} (1 - e^{(\Phi_B - \Phi)/T}) \rangle + \bar{\mu} \frac{\partial^2}{\partial x^2} \bar{v}_y - v_{p_y} p_y \quad . \quad (12)$$

The first term on the rhs is a sheath damping term that drives the potential towards its Bohm value and thus provides a sheath-source for velocity shear in the SOL; the second ($\bar{\mu}$) term serves to diffuse the velocity shear (e.g. from the SOL into the edge plasma), and the third term damps the poloidal (zonal) flows. The sheath and diffusion terms introduce non-locality into the momentum transport model. To a very good approximation, the second term on the lhs can be expressed using quasilinear theory as

$$\langle n v_x v_y \rangle = \bar{n} \langle v_x v_y \rangle + \bar{v}_y \langle n v_x \rangle \quad (13)$$

where $\langle Q \rangle \equiv \bar{Q}$ for any quantity Q . Here, we consider the steady state equation, drop the sheath and diffusion terms, and combine Eqs. (12) and (13) to obtain

$$\frac{\partial}{\partial x} \bar{n} \langle v_x v_y \rangle + \frac{\partial}{\partial x} \bar{v}_y \langle n v_x \rangle = -v_{p_y} p_y \quad . \quad (14)$$

The first term on the lhs is the Reynolds stress term, which drives sheared flows⁴ and the second term describes passive radial convection of the poloidal momentum²⁶ outwards from the edge to the SOL.

Depending on which terms balance in Eq. (14), there are three parameter regimes for turbulent saturation:

(a) For large v_{p_y} , satisfying $\bar{n} |\langle v_x v_y \rangle| / L_x \ll |v_{p_y} p_y|$, Eq. (14) reduces to $v_{p_y} p_y = 0$, and the zonal flows are strongly damped ($\bar{v}_y \rightarrow 0$). In this case, the turbulence saturation occurs by the mechanism of ‘‘plateau formation’’, viz. the strong

turbulent transport modifies the density and temperature profiles, reducing the gradients until the wave-breaking condition is satisfied, as discussed subsequently.

(b) For intermediate values of v_{p_y} , the passive transport term can be neglected when $|\bar{v}_y \langle n v_x \rangle| / L_x < |v_{p_y} p_y|$, and the Reynolds stress is balanced by the damping term. Thus, Eq. (14) reduces to

$$\frac{\partial}{\partial x} \bar{n} \langle v_x v_y \rangle = -v_{p_y} p_y \quad . \quad (15)$$

Here, the turbulence saturation occurs because of the stabilizing effect of the sheared zonal flows. Parameter regimes (a) and (b) correspond to the small and large v_{p_y} limits discussed in Sec. III A, which were illustrated in Figs. 2 and 3.

(c) For $v_{p_y} \approx 0$, i.e. when $|v_{p_y} p_y| \ll |\bar{v}_y \langle n v_x \rangle| / L_x$, the Reynolds stress is balanced in Eq. (14) by the passive (blob) momentum transport term,

$$\frac{\partial}{\partial x} \bar{n} \langle v_x v_y \rangle + \frac{\partial}{\partial x} \bar{v}_y \langle n v_x \rangle = 0 \quad . \quad (16)$$

Here, the sheared flows produced by the Reynold's stress in the edge plasma are transported across the LCS by the passive convection term. This is the bursty regime discussed in Sec. III B. To see this heuristically, we solve an approximate version of Eq. (16) (keeping only the equilibrium gradient terms) for the particle flux:

$$\Gamma \equiv \langle n v_x \rangle = \frac{\bar{n}' \langle v_x v_y \rangle}{\bar{v}_y'} = \frac{\bar{n} \langle v_x v_y \rangle L_v}{\bar{v}_y L_n} \quad . \quad (17)$$

This heuristic argument suggests that the particle flux becomes large as $\bar{v}_y' \rightarrow 0$. In the simulations, a plateau develops in the flow profile as the instability evolves and “zero-shear” points ($\bar{v}_y' \rightarrow 0$) are created in the birth zone (see Fig. 8), causing the bursts of flux, as shown in Fig. 7.

Having briefly surveyed the physics of the three turbulence saturation regimes, we now give a more quantitative treatment of the various saturation mechanisms. Here, we

assume that the turbulent cross-phase gives maximum transport, i.e. $\langle \tilde{n}\tilde{v}_x \rangle \sim |\tilde{n}| |\tilde{v}_x|$, which is true in the present simulations that are dominated by the curvature-driven interchange mode.

In the limit $\nu_{p_y} \rightarrow \infty$, we use the wave-breaking condition in the form $k_y |\tilde{n}| = \nabla_x \bar{n}$, where \bar{n} is the background profile in the linear phase (before there is any turbulent profile modification). The continuity equation relates the density and potential fluctuations, implying $\gamma |\tilde{n}| = k_y |\tilde{\phi}| \nabla_x \bar{n}$. Substituting these relations into the definition of particle flux, $\Gamma = \langle \tilde{n}\tilde{v}_x \rangle \sim k_y |\tilde{n}| |\tilde{\phi}|$, we obtain the following estimate of the saturated particle flux in the strong damping limit,

$$\Gamma_{\text{sat}} \sim k_y |\tilde{n}| |\tilde{\phi}| \sim k_y |\tilde{n}|^2 \frac{|\tilde{\phi}|}{|\tilde{n}|} \sim k_y \left(\frac{\nabla_x \bar{n}}{k_y} \right)^2 \left(\frac{\gamma}{k_y \nabla_x \bar{n}} \right) \sim \gamma \nabla_x \bar{n} / k_y^2 . \quad (18)$$

Thus, the turbulent diffusion coefficient is just the mixing length result, $D = \gamma / k_y^2$. If the turbulence is driven by the curvature-driven interchange mode without significant damping, we can estimate the dimensionless growth rate as $\gamma = (\beta / 2L_n)^{1/2}$, where $\beta = 2\rho_s / R_c$ and R_c is the radius of curvature. For the most highly damped case in Fig. 3, we find that the growth rate in the simulation is significantly lower than this estimate. When the numerically-obtained growth rate is used, the wave-breaking estimate for Γ_{sat} agrees with the computed turbulent flux to within a factor of 3: Eq. (18) gives $\Gamma_{\text{sat}} = 3.2 \times 10^{17} \text{ cm}^{-2} \text{ s}^{-1}$ in dimensional units whereas the particle flux computed in the simulation is $\Gamma_{\text{sat}} = 9.6 \times 10^{17} \text{ cm}^{-2} \text{ s}^{-1}$.

In the limit of small but finite ν_{p_y} (i.e. the intermediate damping case), the condition for sheared flow to stabilize the mode is taken as $\gamma \sim |\bar{v}'_y| \sim |\bar{v}_y| / L_v$. Balancing the Reynolds stress term in the momentum equation with the damping term [Eq. (15)] gives the scaling of the zonal flow, $\bar{v}_y = (k_x / k_y)^2 (k_y^3 |\tilde{\phi}|^2) / \nu_{p_y}$. Combining this result with the shear flow stabilization condition provides an estimate for the saturated fluctuation level, $|\tilde{\phi}|^2 = (\gamma \nu_{p_y} L_y / k_y^3) (k_y / k_x)^2$. Finally, using the continuity equation,

$\gamma|\tilde{n}| = k_y|\tilde{\phi}|\nabla_x\bar{n}$, and the definition of radial particle flux, we obtain an estimate of the saturated particle flux for the intermediate- v_{p_y} case:

$$\Gamma_{\text{sat}} = \langle \tilde{n}\tilde{v}_x \rangle \sim k_y \langle \tilde{n}\tilde{\phi} \rangle \sim \left(\frac{k_y}{k_x}\right)^2 \frac{\bar{n}v_{p_y}L_v}{k_yL_n}. \quad (19)$$

Using reasonable estimates of the simulation parameters for the case $v_{p_y} = 0.005$ (the “knee” of the curve in Fig. 3, we find good agreement with the computed turbulent particle flux, $\Gamma_{\text{sat}} = 6.7 \times 10^{17} \text{ cm}^{-2}\text{s}^{-1}$ in dimensional units.

These estimates for Γ_{sat} also agree qualitatively with the shape of the curve shown in Fig. 3. For small zonal-flow damping, Γ_{sat} is proportional to v_{p_y} and independent of growth rate γ , whereas for large damping Γ_{sat} is independent of v_{p_y} and proportional to γ . Equating the two expressions gives an estimate of the value of v_{p_y} at the knee of the curve which marks the transition between the intermediate and large v_{p_y} regimes:

$$v_{p_y}(\text{knee}) = \left(\frac{k_x}{k_y}\right)^2 \frac{\gamma}{k_yL_v}. \quad (20)$$

The bursty regime, obtained in the absence of damping, requires a more complicated dynamic model and is outside the scope of the present paper.

Finally, we conclude this section with a set of “rules” that appear to describe the dynamical behavior of our simulations of edge turbulence in the non-bursty weak-damping regime:

- (1) the Reynolds stress term $\langle n \rangle \langle v_x v_y \rangle$ acts to increase the magnitude of the velocity shear, $|\bar{v}'_y|$ until it balances the mode growth rate γ . This can be understood from the classic picture of tilted ellipses.^{1,2} It is also related to the usual modulational instability picture of sheared flow generation.¹⁻⁴

- (2) the Reynolds-stress term tries to drive $\bar{v}_y > 0$ inside the LCS, i.e. in the electron (diamagnetic drift) direction
- (3) the sheath term determines the sign of the flow in the SOL, i.e. $\bar{v}_y < 0$, which is the ion (diamagnetic drift) direction.

These three elements combine to determine the velocity shear profile in the simulations.

V. Summary and Discussion

In this paper, we have investigated the interaction of edge turbulence, blob generation, momentum transport and sheared zonal flows in 2D fluid simulations using a Braginskii-type model for the edge and SOL. A control parameter for these studies was the momentum damping rate ν_{p_y} . We have shown that the turbulent flux increases rapidly as ν_{p_y} increases and the zonal flows are damped (see Fig. 3). A more detailed analysis shows that the saturation of edge turbulence has three parameter regimes which correspond to balancing different pairs of terms in the zonally-averaged momentum equation, Eq. (14), as discussed in Sec. IV. For small ν_{p_y} , the turbulence is saturated by sheared flow stabilization and the convective transport occurs via blobs, whereas for large ν_{p_y} the turbulence is saturated by profile modification (sometimes called plateau formation or wave-breaking) and the convective transport occurs via radial streamers. The turbulent transport across the LCS is larger in the latter case-

The dynamics of the sheared zonal flow was shown to be driven by two effects: the turbulent Reynolds stress in the edge, and the sheath-generated sheared flows in the SOL. As the velocity shear, $\bar{v}'_y = d\bar{v}_y/dx$, has opposite signs for the two effects, their competition gives reduced velocity shear in the main interaction region and can lead to bursty transport when \bar{v}'_y is small in this layer. Thus, the turbulence depends on the various sources of edge and SOL dissipation in a complex way. A set of rules was given at the end of Sec. IV, which describes the behavior of the simulations.

Thus, in spite of differences such as lack of scale separation, sheath dissipation, strong turbulence and fast profile modification, the nonlinear saturation of turbulence in the edge and SOL has many features in common with core turbulence. It involves the nonlinear generation of coherent structures (radial streamers and sheared flow layers), which interact by a predator-prey relation and can give rise to bursty transport. However, the edge turbulence interaction is complicated by additional SOL physics such as blob creation and sheath-generated sheared flows. More work is needed to understand the full parameter space for these additional interactions.

Acknowledgements

This work was supported by the U.S. Department of Energy (DOE) under DOE Grant No. DE-FG02-97ER54392; however, this support does not constitute an endorsement by the DOE of the views expressed herein.

Figure Captions

Fig. 1 Schematic of the radial profiles (described in the text) which define the edge and SOL regions.

Fig. 2 (color online) Time history of the particle flux ($\times 10^3$) at the sheath entrance ($\Delta r = 4.4$ cm) in the limit of (a) infinite and (b) zero flow damping. The turbulence is more intermittent in the small damping limit, where the saturation is controlled by the zonal flows.

Fig. 3 (color online) Flux and flow shear vs. the flow damping parameter $\nu_{py} \cdot \langle \Gamma \rangle_{\max}$ is the maximum of the time-averaged radial particle flux, and error bars are the standard deviation of the flux (σ_{Γ}), with respect to time, at the location of that maximum, x_{\max} . $\langle |\xi| \rangle$ is the time-averaged magnitude of the shear, averaged over $x < x_{\max}$, and error bars are the standard deviation of the shear with respect to time, averaged over $x < x_{\max}$. Both quantities are normalized by their maxima ($\langle \Gamma \rangle_{\max} = 9.6 \times 10^{17} \text{ cm}^{-2} \text{ s}^{-1}$ and $\xi_{\max} = 4.7 \times 10^4 \text{ s}^{-1}$) to aid illustration.

Fig. 4 (a) Legislated flow shear profile described in the text. (b) Poloidally-averaged radial flux, Γ ($\times 400$), at the sheath entrance ($\Delta r = 4.4$ cm) and shear, ξ ($\times 400$), at $\Delta r = -2$ cm, where the amplitude of the perturbation in (a) is maximized. The shear profiles in (a) are at times indicated by the symbols in (b). This numerical experiment demonstrates that the turbulence is stabilized by the sheared flows in the $\nu_{py} = 0$ limit.

Fig. 5 (color online) Plot of the average density profile $\langle \bar{n}(\Delta r) \rangle_t$ for several values of the flow dissipation parameter ν_{py} . The degree of dissipation used in the simulation is indicated by the color of the curve, and the color scheme corresponds to that used in Fig. 3. The vertical dashed line indicates the nominal position of the LCS.

Fig. 6 Time history of the zonally-averaged radial particle flux $\Gamma(t)$ at the entrance to the sheath ($\Delta r = 4.4 \text{ cm}$) for two values of the core-side boundary potential.

Fig. 7 (color online) A time slice of a simulation near marginality ($\overline{\Phi}(0) = 10$) showing the history of the particle flux (Γ), velocity shear $\xi = d\overline{v}_y/dx$ and pressure gradient at $\Delta r = -2 \text{ cm}$. Note the bursts in the particle flux when the velocity shear vanishes. Compare with Fig. 4.

Fig. 8 Radial profile of the velocity shear $\xi = d\overline{v}_y/dx$ at times before and including the second burst in Fig. 7: (a) 4580 μs , (b) 4620 μs and (c) 4650 μs .

References

- ¹ P. W. Terry, *Rev. Mod. Phys.*, **72**, 109 (2000).
- ² P. H. Diamond, S.-I. Itoh, K. Itoh and T. S. Hahm, *Plasma Phys. Control. Fusion* **47**, R35 (2005).
- ³ A. Fujisawa, *Nucl. Fusion* **49**, 013001 (2009)
- ⁴ P.H. Diamond, S. Champeaux, M. Malkov, A. Das, I. Gruzinov, M.N. Rosenbluth, C. Holland, B. Wecht, A.I. Smolyakov, F.L. Hinton, Z. Lin, T.S. Hahm, *Nucl. Fusion* **41**, 1067 (2001).
- ⁵ P. Beyer, S. Benkadda, X. Garbet and P. H. Diamond, *Phys. Rev. Lett.* **85**, 4892 (2000).
- ⁶ S. Benkadda, P. Beyer, N. Bian, C. Figarella, O. Garcia, X. Garbet, P. Ghendrih, Y. Sarazin, P.H. Diamond, *Nucl. Fusion* **41**, 995 (2001).
- ⁷ J. A. Boedo, D. Rudakov, R. Moyer, S. Krasheninnikov, D. Whyte, G. McKee, G. Tynan, M. Schaffer, P. Stangeby, P. West, S. Allen, T. Evans, R. Fonck, E. Hollmann, A. Leonard, A. Mahdavi, G. Porter, M. Tillack, and G. Antar, *Phys. Plasmas* **8**, 4826 (2001).
- ⁸ D L Rudakov, J A Boedo, R A Moyer, S Krasheninnikov, A W Leonard, M A Mahdavi, G R McKee, G D Porter, P C Stangeby, J G Watkins, W P West, D G Whyte and G Antar, *Plasma Phys. Control. Fusion* **44**, 717 (2002).
- ⁹ S.J. Zweben, R.J. Maqueda, D.P. Stotler, A. Keesee, J. Boedo, C.E. Bush, S.M. Kaye, B. LeBlanc, J.L. Lowrance, V.J. Mastrocola, R. Maingi, N. Nishino, G. Renda, D.W. Swain, J.B. Wilgen and the NSTX Team, *Nucl. Fusion* **44**, 134 (2004).
- ¹⁰ B. LaBombard, J.W. Hughes, D. Mossessian, M. Greenwald, B. Lipschultz, J.L. Terry and the Alcator C-Mod Team, *Nucl. Fusion* **45**, 1658 (2005).
- ¹¹ J.L. Terry, N.P. Basse, I. Cziegler, M. Greenwald, O. Grulke, B. LaBombard, S.J. Zweben, E.M. Edlund, J.W. Hughes, L. Lin, Y. Lin, M. Porkolab, M. Sampsell, B. Veto and S.J. Wukitch, *Nucl. Fusion* **45** 1321, (2005).
- ¹² G. R. Tynan, C. Holland, J. H. Yu, A. James, D. Nishijima, M. Shimada, and N. Taheri, *Plasma Phys. Control. Fusion* **48**, S51 (2006); C. Holland, J. H. Yu, A. James, D. Nishijima, N. Taheri, and G. R. Tynan, *Phys. Rev. Lett.* **96**, 195002 (2006).
- ¹³ M. Vergote, M. Van Schoor, Y. Xu, S. Jachmich, and R. Weynants, *Plasma Phys. Control. Fusion* **48**, S75 (2006).
- ¹⁴ A. Fasoli, B. Labit, M. McGrath, S. H. Müller, G. Plyushchev, M. Podestà, and F. M. Poli, *Phys. Plasmas* **13**, 055902 (2006)

- ¹⁵ S. H. Müller, A. Diallo, A. Fasoli, I. Furno, B. Labit, and M. Podestà, *Phys. Plasmas* **14**, 110704 (2007).
- ¹⁶ M. Agostini, S. J. Zweben, R. Cavazzana, P. Scarin, G. Serianni, R. J. Maqueda, and D. P. Stotler, *Phys. Plasmas* **14**, 102305 (2007).
- ¹⁷ B. LaBombard, J. W. Hughes, N. Smick, A. Graf, K. Marr, R. McDermott, M. Reinke, M. Greenwald, B. Lipschultz, J. L. Terry, D. G. Whyte, S. J. Zweben, and Alcator C-Mod Team, *Phys. Plasmas* **15**, 056106 (2008).
- ¹⁸ Z. Yan, J. H. Yu, C. Holland, M. Xu, S. H. Müller, and G. R. Tynan, *Phys. Plasmas* **15**, 092309 (2008).
- ¹⁹ A. Diallo, A. Fasoli, I. Furno, B. Labit, M. Podesta and C. Theiler, *Phys. Rev. Lett.* **101**, 115005 (2008).
- ²⁰ P. N. Guzdar, J. F. Drake, D. McCarthy, A. B. Hassam, and C. S. Liu, *Phys. Fluids B* **5**, 3712 (1993).
- ²¹ A. Das, A. Sen, S. Mahajan, and P. Kaw, *Phys. Plasmas* **8**, 5104 (2001).
- ²² O. Garcia, N. H. Bian, J-V Paulsen, S. Benkadda, and K. Rypdal, *Plasma Phys. Control. Fusion* **45** 919 (2003).
- ²³ G. L. Falchetto, Y. Sarazin, X. Garbet, Ph. Ghendrih, M. Ottaviani, S. Benkadda, and P. Beyer, in *Proceedings of the 20th IAEA Fusion Energy Conference*, November 1-6, 2004, Vilamoura, Portugal (2004), paper TH/1-3Rd.
- ²⁴ N. Bisai, A. Das, S. Deshpande, R. Jha, P. Kaw, A. Sen, and R. Singh, *Phys. Plasmas* **12**, 072520 (2005); N. Bisai, A. Das, S. Deshpande, R. Jha, P. Kaw, A. Sen, and R. Singh, *Phys. Plasmas* **12**, 102515 (2005).
- ²⁵ N. Kasuya, M. Yagi, K. Itoh, and S-I Itoh, *Phys. Plasmas* **15**, 052302 (2008).
- ²⁶ J. R. Myra, D. A. Russell, and D. A. D'Ippolito, *Phys. Plasmas* **15**, 032304 (2008).
- ²⁷ P. Ricci, B. N. Rogers and S. Brunner, *Phys. Rev. Lett.* **100**, 225002 (2008).
- ²⁸ S. J. Zweben, J. A. Boedo, O. Grulke, C. Hidalgo, B. LaBombard, R. J. Maqueda, P. Scarin, and J L Terry, *Plasma Phys. Control. Fusion* **49**, S1 (2007).
- ²⁹ S. I. Krasheninnikov, *Phys. Lett. A* **283**, 368 (2001).
- ³⁰ D. A. D'Ippolito, J. R. Myra, and S. I. Krasheninnikov, *Phys. Plasmas* **9**, 222 (2002).
- ³¹ S. I. Krasheninnikov, D. A. D'Ippolito, J. R. Myra, *J. Plasma Phys.* **74**, 679 (2008).
- ³² J. R. Myra, D. A. Russell, and D. A. D'Ippolito, *Phys. Plasmas* **13**, 112502 (2006).
- ³³ D. A. Russell, J. R. Myra and D. A. D'Ippolito, *Phys. Plasmas* **14**, 102307 (2007).

- ³⁴ G.L. Falchetto, Y. Sarazin, X. Garbet, Ph. Ghendrih, M. Ottaviani, S. Benkadda, P. Beyer, 20th IAEA Fusion Energy Conf, Vilamoura, Portugal, 2004 (IAEA, Vienna, 2004), paper IAEA-CN-116/TH/1-3Rd.
- ³⁵ M. Wakatani and A. Hasegawa, *Phys. Fluids* **27**, 611 (1984); A. Hasegawa and M. Wakatani *Phys. Rev. Lett.* **59**, 1581 (1987).
- ³⁶ M. Ono, S.M. Kaye, Y.-K.M. Peng, G. Barnes, W. Blanchard, M.D. Carter, J. Chrzanowski, L. Dudek, R. Ewig, D. Gates, R.E. Hatcher, T. Jarboe, S.C. Jardin, D. Johnson, R. Kaita, M. Kalish, C.E. Kessel, H.W. Kugel, R. Maingi, R. Majeski, J. Manickam, B. McCormack, J. Menard, D. Mueller, B.A. Nelson, B.E. Nelson, C. Neumeyer, G. Oliaro, F. Paoletti, R. Parsells, E. Perry, N. Pomphrey, S. Ramakrishnan, R. Raman, G. Rewoldt, J. Robinson, A.L. Roquemore, P. Ryan, S. Sabbagh, D. Swain, E.J. Synakowski, M. Viola, M. Williams, J.R. Wilson and NSTX Team, *Nucl. Fusion* **40**, 557 (2000).
- ³⁷ J. R. Myra. and D. A. D'Ippolito, *Phys. Plasmas* **12**, 092511 (2005).
- ³⁸ D. A. D'Ippolito, J. Boedo , D. P. Lundberg, R. Maqueda, J. R. Myra, D. A. Russell, D. P. Stotler and S. J. Zweben, in *Plasma Physics and Controlled Nuclear Fusion Research 2008* (IAEA, Vienna, 2009), paper IAEA-CN-165-TH/P4-17.

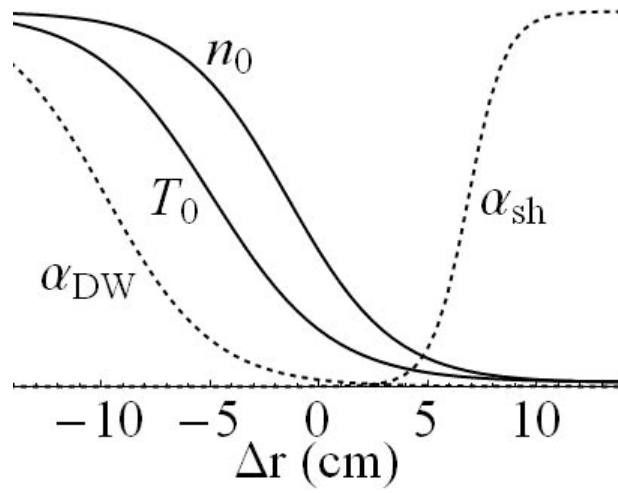


Fig. 1 Schematic of the radial profiles (described in the text) which define the edge and SOL regions.

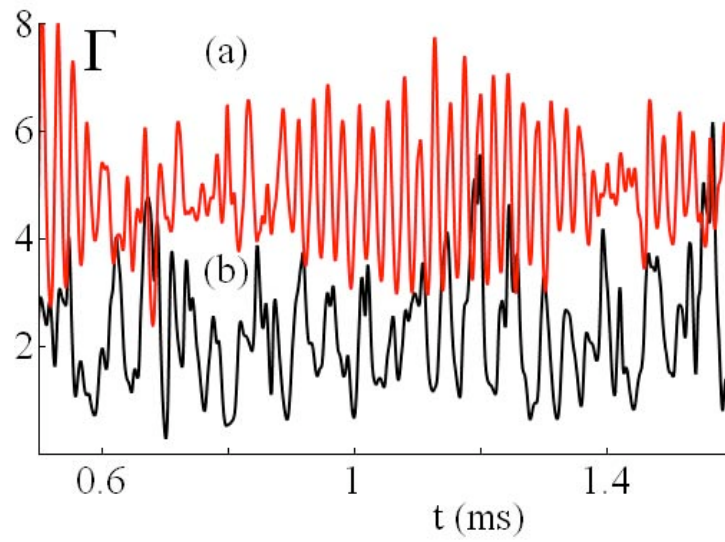


Fig. 2 (color online) Time history of the particle flux ($\times 10^3$) at the sheath entrance ($\Delta r = 4.4$ cm) in the limit of (a) infinite and (b) zero flow damping. The turbulence is more intermittent in the small damping limit, where the saturation is controlled by the zonal flows.

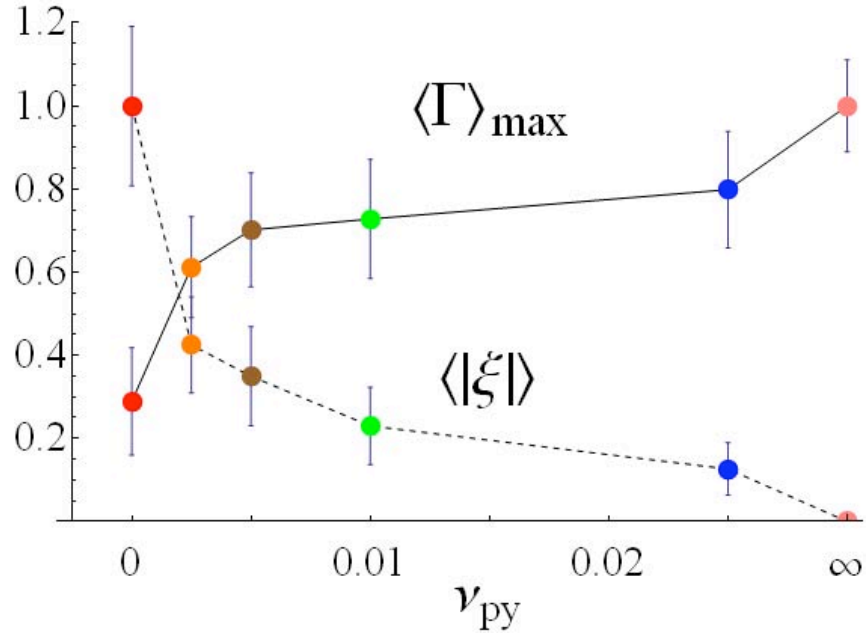


Fig. 3 (color online) Flux and flow shear vs. the flow damping parameter ν_{py} . $\langle \Gamma \rangle_{\max}$ is the maximum of the time-averaged radial particle flux, and error bars are the standard deviation of the flux (σ_{Γ}), with respect to time, at the location of that maximum, x_{\max} . $\langle |\xi| \rangle$ is the time-averaged magnitude of the shear, averaged over $x < x_{\max}$, and error bars are the standard deviation of the shear with respect to time, averaged over $x < x_{\max}$. Both quantities are normalized by their maxima ($\langle \Gamma \rangle_{\max} = 9.6 \times 10^{17} \text{ cm}^{-2} \text{ s}^{-1}$ and $\xi_{\max} = 4.7 \times 10^4 \text{ s}^{-1}$) to aid illustration.

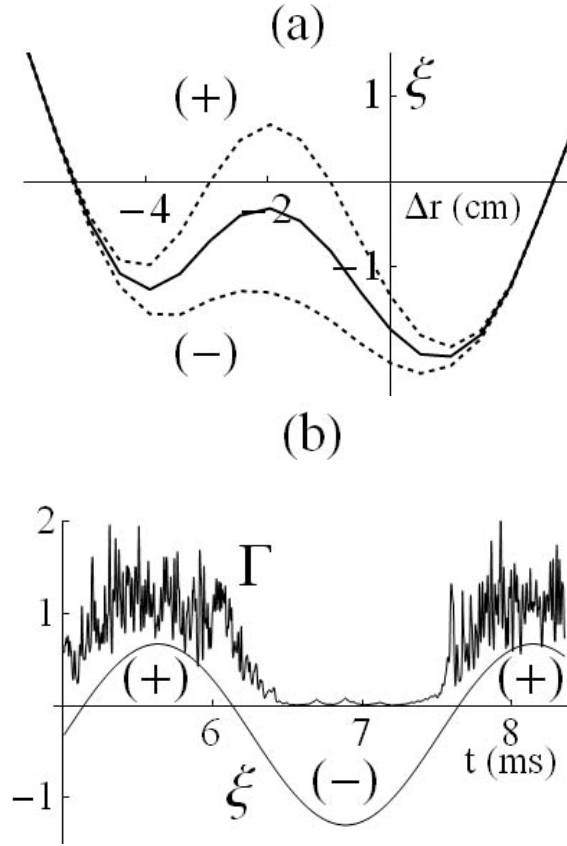


Fig. 4 (a) Legislated flow shear profile described in the text. (b) Poloidally-averaged radial flux, Γ ($\times 400$), at the sheath entrance ($\Delta r = 4.4$ cm) and shear, ξ ($\times 400$), at $\Delta r = -2$ cm, where the amplitude of the perturbation in (a) is maximized. The shear profiles in (a) are at times indicated by the symbols in (b). This numerical experiment demonstrates that the turbulence is stabilized by the sheared flows in the $v_{py} = 0$ limit.

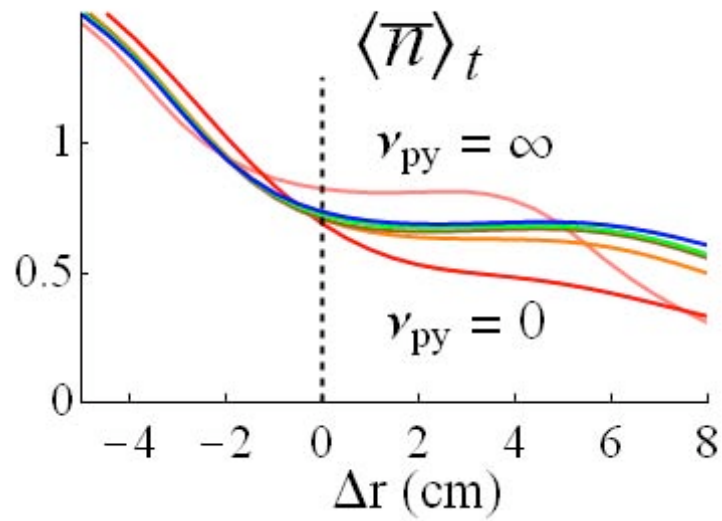


Fig. 5 (color online) Plot of the average density profile $\langle \bar{n}(\Delta r) \rangle_t$ for several values of the flow dissipation parameter ν_{py} . The degree of dissipation used in the simulation is indicated by the color of the curve, and the color scheme corresponds to that used in Fig. 3. The vertical dashed line indicates the nominal position of the LCS.

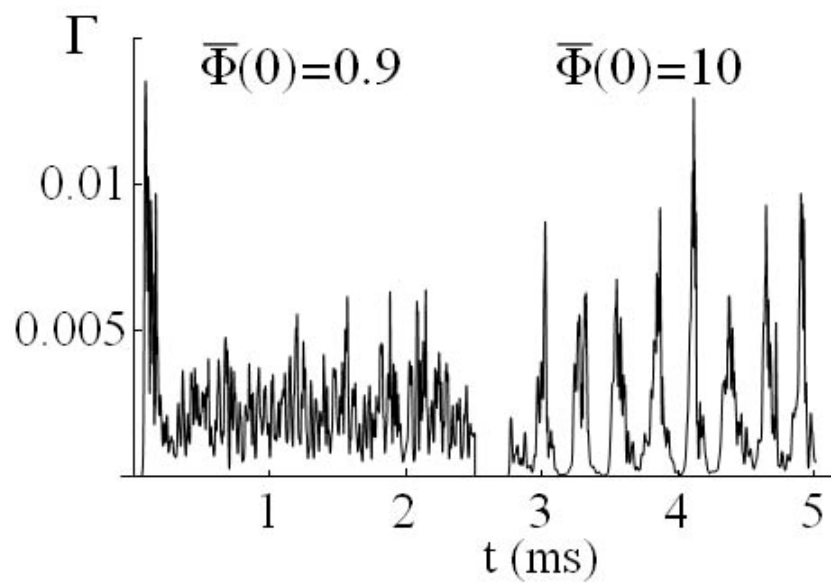


Fig. 6 Time history of the zonally-averaged radial particle flux $\Gamma(t)$ at the entrance to the sheath ($\Delta r = 4.4$ cm) for two values of the core-side boundary potential.

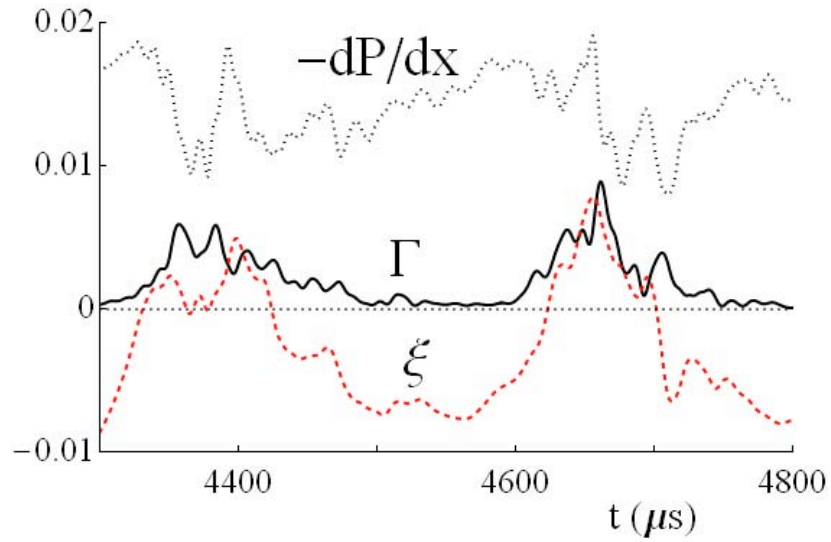


Fig. 7 (color online) A time slice of a simulation near marginality ($\bar{\Phi}(0) = 10$) showing the history of the particle flux (Γ), velocity shear $\xi = d\bar{v}_y/dx$ and pressure gradient at $\Delta r = -2$ cm. Note the bursts in the particle flux when the velocity shear vanishes. Compare with Fig. 4.

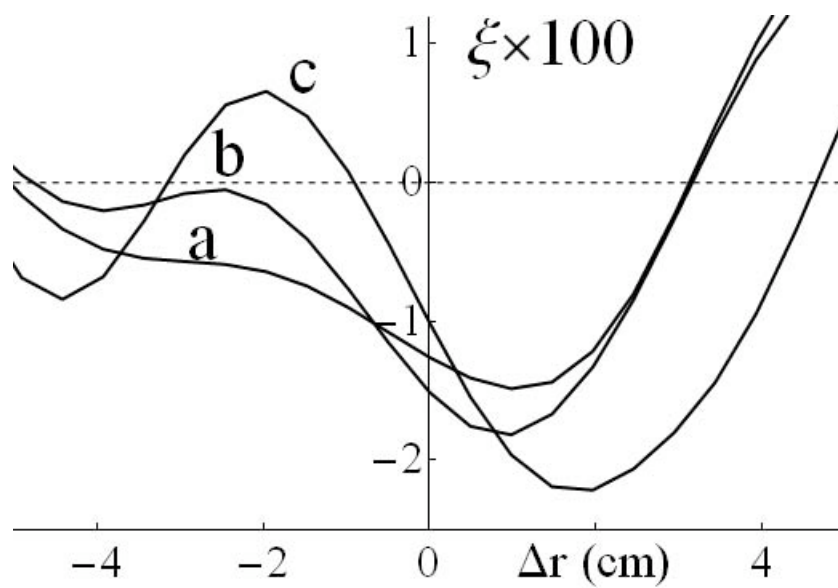


Fig. 8 Radial profile of the velocity shear $\xi = d\bar{v}_y/dx$ at times before and including the second burst in Fig. 7: (a) 4580 μ s, (b) 4620 μ s and (c) 4650 μ s.